Fiber-bundle microendoscopy with sub-diffuse reflectance spectroscopy and intensity mapping for multimodal optical biopsy of stratified epithelium

Gage J. Greening,[1,*] Haley M. James,[2] Amy J. Powless,[1] Joshua A. Hutcheson,[1] Mary K. Dierks,[3] Narasimhan Rajaram,[1] and Timothy J. Muldoon[1]

[1]*Department of Biomedical Engineering, University of Arkansas, 1 University of Arkansas, Fayetteville, AR 72701, USA*

[2]*Department of Chemistry and Biochemistry, University of Arkansas, 1 University of Arkansas, Fayetteville, AR 72701, USA*

[3]*Department of Biological Sciences, University of Arkansas, 1 University of Arkansas, Fayetteville, AR 72701, USA*

**ggreenin@uark.edu*

Abstract: Early detection of structural or functional changes in dysplastic epithelia may be crucial for improving long-term patient care. Recent work has explored myriad non-invasive or minimally invasive "optical biopsy" techniques for diagnosing early dysplasia, such as high-resolution microendoscopy, a method to resolve sub-cellular features of apical epithelia, as well as broadband sub-diffuse reflectance spectroscopy, a method that evaluates bulk health of a small volume of tissue. We present a multimodal fiber-based microendoscopy technique that combines high-resolution microendoscopy, broadband (450-750 nm) sub-diffuse reflectance spectroscopy (sDRS) at two discrete source-detector separations (374 and 730 μm), and sub-diffuse reflectance intensity mapping (sDRIM) using a 635 nm laser. Spatial resolution, magnification, field-of-view, and sampling frequency were determined. Additionally, the ability of the sDRS modality to extract optical properties over a range of depths is reported. Following this, proof-of-concept experiments were performed on tissue-simulating phantoms made with poly(dimethysiloxane) as a substrate material with cultured MDA-MB-468 cells. Then, all modalities were demonstrated on a human melanocytic nevus from a healthy volunteer and on resected colonic tissue from a murine model. Qualitative *in vivo* image data is correlated with reduced scattering and absorption coefficients.

OCIS codes: (120.4640) Optical instruments; (060.2310) Fiber optics; (170.6510) Spectroscopy, tissue diagnostics; (110.2945) Illumination design; (170.2150) Endoscopic imaging.

References and links

1. P. Sharma and E. Montgomery, "Gastrointestinal dysplasia," Pathology **45**(3), 273–285 (2013).
2. P. M. Speight, "Update on oral epithelial dysplasia and progression to cancer," Head Neck Pathol. **1**(1), 61–66 (2007).
3. Y. Zhang, "Epidemiology of esophageal cancer," World J. Gastroenterol. **19**(34), 5598–5606 (2013).
4. N. Harpaz and A. D. Polydorides, "Colorectal dysplasia in chronic inflammatory bowel disease: pathology, clinical implications, and pathogenesis," Arch. Pathol. Lab. Med. **134**(6), 876–895 (2010).
5. M. Ponz de Leon and C. Di Gregorio, "Pathology of colorectal cancer," Dig. Liver Dis. **33**(4), 372–388 (2001).
6. M. J. Arends, C. H. Buckley, and M. Wells, "Aetiology, pathogenesis, and pathology of cervical neoplasia," J. Clin. Pathol. **51**(2), 96–103 (1998).
7. S. J. Hwang and K. R. Shroyer, "Biomarkers of Cervical Dysplasia and Carcinoma," J. Oncol. **2012**, 507286 (2012).

#247300 Received 4 Aug 2015; revised 14 Oct 2015; accepted 14 Nov 2015; published 19 Nov 2015

8. R. S. Dacosta, B. C. Wilson, and N. E. Marcon, "New optical technologies for earlier endoscopic diagnosis of premalignant gastrointestinal lesions," J. Gastroenterol. Hepatol. **17**, S85–S104 (2002).
9. T. J. Muldoon, D. Roblyer, M. D. Williams, V. M. T. Stepanek, R. Richards-Kortum, and A. M. Gillenwater, "Noninvasive imaging of oral neoplasia with a high-resolution fiber-optic microendoscope," Head Neck **34**(3), 305–312 (2012).
10. H. D. Appelman, "What is dysplasia in the gastrointestinal tract?" Arch. Pathol. Lab. Med. **129**(2), 170–173 (2005).
11. M. Gu, H. Bao, and H. Kang, "Fibre-optical microendoscopy," J. Microsc. **254**(1), 13–18 (2014).
12. T. J. Muldoon, M. C. Pierce, D. L. Nida, M. D. Williams, A. Gillenwater, and R. Richards-Kortum, "Subcellular-resolution molecular imaging within living tissue by fiber microendoscopy," Opt. Express **15**(25), 16413–16423 (2007).
13. M. C. Pierce, Y. Guan, M. K. Quinn, X. Zhang, W. H. Zhang, Y. L. Qiao, P. Castle, and R. Richards-Kortum, "A pilot study of low-cost, high-resolution microendoscopy as a tool for identifying women with cervical precancer," Cancer Prev. Res. (Phila.) **5**(11), 1273–1279 (2012).
14. M. Pierce, D. Yu, and R. Richards-Kortum, "High-resolution fiber-optic microendoscopy for in situ cellular imaging," J. Vis. Exp. **47**, e2306 (2011).
15. M. K. Quinn, T. C. Bubi, M. C. Pierce, M. K. Kayembe, D. Ramogola-Masire, and R. Richards-Kortum, "High-resolution microendoscopy for the detection of cervical neoplasia in low-resource settings," PLoS One **7**(9), e44924 (2012).
16. S. S. Chang, R. Shukla, A. D. Polydorides, P. M. Vila, M. Lee, H. Han, P. Kedia, J. Lewis, S. Gonzalez, M. K. Kim, N. Harpaz, J. Godbold, R. Richards-Kortum, and S. Anandasabapathy, "High resolution microendoscopy for classification of colorectal polyps," Endoscopy **45**(7), 553–559 (2013).
17. P. A. Keahey, T. S. Tkaczyk, K. M. Schmeler, and R. R. Richards-Kortum, "Optimizing modulation frequency for structured illumination in a fiber-optic microendoscope to image nuclear morphometry in columnar epithelium," Biomed. Opt. Express **6**(3), 870–880 (2015).
18. N. D. Parikh, D. Perl, M. H. Lee, B. Shah, Y. Young, S. S. Chang, R. Shukla, A. D. Polydorides, E. Moshier, J. Godbold, E. Zhou, J. Mitcham, R. Richards-Kortum, and S. Anandasabapathy, "In vivo diagnostic accuracy of high-resolution microendoscopy in differentiating neoplastic from non-neoplastic colorectal polyps: a prospective study," Am. J. Gastroenterol. **109**(1), 68–75 (2014).
19. S. P. Prieto, A. J. Powless, J. W. Boice, S. G. Sharma, and T. J. Muldoon, "Proflavine Hemisulfate as a Fluorescent Contrast Agent for Point-of-Care Cytology," PLoS One **10**(5), e0125598 (2015).
20. D. R. Rivera, C. M. Brown, D. G. Ouzounov, I. Pavlova, D. Kobat, W. W. Webb, and C. Xu, "Compact and flexible raster scanning multiphoton endoscope capable of imaging unstained tissue," Proc. Natl. Acad. Sci. U.S.A. **108**(43), 17598–17603 (2011).
21. W. Piyawattanametha and T. D. Wang, "MEMS-Based Dual Axes Confocal Microendoscopy," IEEE J. Sel. Top. Quantum Electron. **16**(4), 804–814 (2010).
22. X. Chen, X. Xu, D. T. McCormick, K. Wong, and S. T. C. Wong, "Multimodal nonlinear endo-microscopy probe design for high resolution, label-free intraoperative imaging," Biomed. Opt. Express **6**(7), 2283–2293 (2015).
23. S. C. Kanick, D. M. McClatchy 3rd, V. Krishnaswamy, J. T. Elliott, K. D. Paulsen, and B. W. Pogue, "Sub-diffusive scattering parameter maps recovered using wide-field high-frequency structured light imaging," Biomed. Opt. Express **5**(10), 3376–3390 (2014).
24. S. C. Kanick, D. J. Robinson, H. J. Sterenborg, and A. Amelink, "Monte Carlo analysis of single fiber reflectance spectroscopy: photon path length and sampling depth," Phys. Med. Biol. **54**(22), 6991–7008 (2009).
25. R. Hennessy, W. Goth, M. Sharma, M. K. Markey, and J. W. Tunnell, "Effect of probe geometry and optical properties on the sampling depth for diffuse reflectance spectroscopy," J. Biomed. Opt. **19**(10), 107002 (2014).
26. J. L. Jayanthi, G. U. Nisha, S. Manju, E. K. Philip, P. Jeemon, K. V. Baiju, V. T. Beena, and N. Subhash, "Diffuse reflectance spectroscopy: diagnostic accuracy of a non-invasive screening technique for early detection of malignant changes in the oral cavity," BMJ Open **1**(1), e000071 (2011).
27. G. Zonios, L. T. Perelman, V. Backman, R. Manoharan, M. Fitzmaurice, J. Van Dam, and M. S. Feld, "Diffuse reflectance spectroscopy of human adenomatous colon polyps in vivo," Appl. Opt. **38**(31), 6628–6637 (1999).
28. N. M. Marín, A. Milbourne, H. Rhodes, T. Ehlen, D. Miller, L. Benedet, R. Richards-Kortum, and M. Follen, "Diffuse reflectance patterns in cervical spectroscopy," Gynecol. Oncol. **99**(3 Suppl 1), S116–S120 (2005).
29. N. Rajaram, J. S. Reichenberg, M. R. Migden, T. H. Nguyen, and J. W. Tunnell, "Pilot clinical study for quantitative spectral diagnosis of non-melanoma skin cancer," Lasers Surg. Med. **42**(10), 716–727 (2010).
30. G. J. Greening, A. J. Powless, J. A. Hutcheson, S. P. Prieto, A. A. Majid, and T. J. Muldoon, "Design and validation of a diffuse reflectance and spectroscopic microendoscope with poly(dimethylsiloxane)-based phantoms," Proc. SPIE **9332**, 93320R (2015).
31. Y. Guo, Z. Zhang, D. H. Kim, W. Li, J. Nicolai, D. Procissi, Y. Huan, G. Han, R. A. Omary, and A. C. Larson, "Photothermal ablation of pancreatic cancer cells with hybrid iron-oxide core gold-shell nanoparticles," Int. J. Nanomedicine **8**, 3437–3446 (2013).
32. B. W. Pogue and M. S. Patterson, "Review of tissue simulating phantoms for optical spectroscopy, imaging and dosimetry," J. Biomed. Opt. **11**(4), 041102 (2006).
33. M. Wang, S. Shen, J. Yang, E. Bong, and R. Xu, "3D printing method for freeform fabrication of optical phantoms simulating heterogeneous biological tissue," Proc. SPIE **8945**, 894509 (2014).

#247300 Received 4 Aug 2015; revised 14 Oct 2015; accepted 14 Nov 2015; published 19 Nov 2015

34. G. J. Greening, R. Istfan, L. M. Higgins, K. Balachandran, D. Roblyer, M. C. Pierce, and T. J. Muldoon, “Characterization of thin poly(dimethylsiloxane)-based tissue-simulating phantoms with tunable reduced scattering and absorption coefficients at visible and near-infrared wavelengths,” J. Biomed. Opt. **19**(11), 115002 (2014).
35. N. Rajaram, A. Gopal, X. Zhang, and J. W. Tunnell, “Experimental validation of the effects of microvasculature pigment packaging on in vivo diffuse reflectance spectroscopy,” Lasers Surg. Med. **42**(7), 680–688 (2010).
36. A. M. Winkler, P. F. S. Rice, R. A. Drezek, and J. K. Barton, “Quantitative tool for rapid disease mapping using optical coherence tomography images of azoxymethane-treated mouse colon,” J. Biomed. Opt. **15**(4), 041512 (2010).
37. M. R. Keenan, S. J. Leung, P. S. Rice, R. A. Wall, and J. K. Barton, “Dual optical modality endoscopic imaging of cancer development in the mouse colon,” Lasers Surg. Med. **47**(1), 30–39 (2015).
38. V. Turzhitsky, A. Radosevich, J. D. Rogers, A. Taflove, and V. Backman, “A predictive model of backscattering at subdiffusion length scales,” Biomed. Opt. Express **1**(3), 1034–1046 (2010).
39. N. Rajaram, T. H. Nguyen, and J. W. Tunnell, “Lookup table-based inverse model for determining optical properties of turbid media,” J. Biomed. Opt. **13**(5), 050501 (2008).
40. N. Rajaram, T. J. Aramil, K. Lee, J. S. Reichenberg, T. H. Nguyen, and J. W. Tunnell, “Design and validation of a clinical instrument for spectral diagnosis of cutaneous malignancy,” Appl. Opt. **49**(2), 142–152 (2010).
41. S. A. Prahl, *Optical Absorption of Hemoglobin* (O.M.L. Center, 1999).
42. S. L. Jacques, *Optical Absorption of Melanin* (O.M.L. Center, 2015).
43. A. J. Gomes, V. Turzhitsky, S. Ruderman, and V. Backman, “Monte Carlo model of the penetration depth for polarization gating spectroscopy: influence of illumination-collection geometry and sample optical properties,” Appl. Opt. **51**(20), 4627–4637 (2012).
44. S. C. Kanick, H. J. Sterenborg, and A. Amelink, “Empirical model description of photon path length for differential path length spectroscopy: combined effect of scattering and absorption,” J. Biomed. Opt. **13**(6), 064042 (2008).
45. V. Kiisk, “An educational spectrograph using a digital camera as a training aid for physics students,” Eur. J. Phys. **35**(3), 035013 (2014).
46. G. Zonios, A. Dimou, I. Bassukas, D. Galaris, A. Tsolakidis, and E. Kaxiras, “Melanin absorption spectroscopy: new method for noninvasive skin investigation and melanoma detection,” J. Biomed. Opt. **13**(1), 014017 (2008).
47. S. H. Tseng, P. Bargo, A. Durkin, and N. Kollias, “Chromophore concentrations, absorption and scattering properties of human skin in-vivo,” Opt. Express **17**(17), 14599–14617 (2009).
48. A. R. Moser, H. C. Pitot, and W. F. Dove, “A dominant mutation that predisposes to multiple intestinal neoplasia in the mouse,” Science **247**(4940), 322–324 (1990).
49. L. K. Su, K. W. Kinzler, B. Vogelstein, A. C. Preisinger, A. R. Moser, C. Luongo, K. A. Gould, and W. F. Dove, “Multiple intestinal neoplasia caused by a mutation in the murine homolog of the APC gene,” Science **256**(5057), 668–670 (1992).
50. B. O. Karim and D. L. Huso, “Mouse models for colorectal cancer,” Am. J. Cancer Res. **3**(3), 240–250 (2013).
51. L. Lim, B. Nichols, N. Rajaram, and J. W. Tunnell, “Probe pressure effects on human skin diffuse reflectance and fluorescence spectroscopy measurements,” J. Biomed. Opt. **16**(1), 011012 (2011).
52. H. Shangguan, S. A. Prahl, S. L. Jacques, L. W. Casperson, and K. E. Gregory, “Pressure Effects on Soft Tissues Monitored by Changes in Tissue Optical Properties,” SPIE Proceedings of Laser-Tissue Interaction IX, 3254, 366–371 (1998).
53. C. R. Simpson, M. Kohl, M. Essenpreis, and M. Cope, “Near-infrared optical properties of ex vivo human skin and subcutaneous tissues measured using the Monte Carlo inversion technique,” Phys. Med. Biol. **43**(9), 2465–2478 (1998).
54. A. Siegman, “Fresnel reflection, lenserfreflection and evanescent gain,” Opt. Photonics News **21**(1), 38–45 (2010).
55. J. L. Sandell and T. C. Zhu, “A review of in-vivo optical properties of human tissues and its impact on PDT,” J. Biophotonics **4**(11-12), 773–787 (2011).
56. A. N. Bashkatov, E. A. Genina, V. I. Kochubey, V. S. Rubtsov, E. A. Kolesnikova, and V. V. Tuchin, “Optical properties of human colon tissues in the 350 – 2500 nm spectral range,” Quantum Electron. **44**(8), 779–784 (2014).
57. H. J. Wei, D. Xing, G. Y. Wu, H. M. Gu, J. J. Lu, Y. Jin, and X. Y. Li, “Differences in optical properties between healthy and pathological human colon tissues using a Ti:sapphire laser: an in vitro study using the Monte Carlo inversion technique,” J. Biomed. Opt. **10**(4), 044022 (2005).
58. R. A. Wall and J. K. Barton, “Oblique incidence reflectometry: optical models and measurements using a side-viewing gradient index lens-based endoscopic imaging system,” J. Biomed. Opt. **19**(6), 067002 (2014).
59. M. Martinelli, A. Gardner, D. Cuccia, C. Hayakawa, J. Spanier, and V. Venugopalan, “Analysis of single Monte Carlo methods for prediction of reflectance from turbid media,” Opt. Express **19**(20), 19627–19642 (2011).
60. F. van Leeuwen-van Zaane, U. A. Gamm, P. B. A. A. van Driel, T. J. A. Snoeks, H. S. de Bruijn, A. van der Ploeg-van den Heuvel, I. M. Mol, C. W. G. M. Löwik, H. J. Sterenborg, A. Amelink, and D. J. Robinson, “In vivo quantification of the scattering properties of tissue using multi-diameter single fiber reflectance spectroscopy,” Biomed. Opt. Express **4**(5), 696–708 (2013).
61. I. V. Meglinski and S. J. Matcher, “Quantitative assessment of skin layers absorption and skin reflectance spectra simulation in the visible and near-infrared spectral regions,” Physiol. Meas. **23**(4), 741–753 (2002).

#247300 Received 4 Aug 2015; revised 14 Oct 2015; accepted 14 Nov 2015; published 19 Nov 2015

62. A. Garcia-Uribe, E. B. Smith, J. Zou, M. Duvic, V. Prieto, and L. V. Wang, "In-vivo characterization of optical properties of pigmented skin lesions including melanoma using oblique incidence diffuse reflectance spectrometry," J. Biomed. Opt. **16**(2), 020501 (2011).
63. M. C. Pierce, R. A. Schwarz, V. S. Bhattar, S. Mondrik, M. D. Williams, J. J. Lee, R. Richards-Kortum, and A. M. Gillenwater, "Accuracy of in vivo multimodal optical imaging for detection of oral neoplasia," Cancer Prev. Res. (Phila.) **5**(6), 801–809 (2012).
64. J. M. Jabbour, M. A. Saldua, J. N. Bixler, and K. C. Maitland, "Confocal endomicroscopy: instrumentation and medical applications," Ann. Biomed. Eng. **40**(2), 378–397 (2012).
65. Y. Yamada and H. Mori, "Multistep carcinogenesis of the colon in ApcMin/+ mouse," Cancer Sci. **98**(1), 6–10 (2007).

---

1. Introduction

Gastrointestinal dysplasia is an abnormal but non-invasive proliferation of cells in the gastrointestinal epithelium that, when diagnosed, is assumed to progress to carcinoma [1, 2]. In the oral cavity and esophagus, dysplasia can potentially become squamous cell carcinoma (SCC) or adenocarcinoma, cancer of the stratified squamous epithelium or columnar glandular cells, respectively [2]. Most adenocarcinomas arise from dysplastic changes associated with Barrett's esophagus, although SCC is more prevalent in the upper digestive tract worldwide [3]. In the colorectal region, dysplasia can form adenomatous polyps which become invasive upon penetration into the submucosa [4, 5]. Dysplasia can also arise in the epithelia of other organs. For example, cervical dysplasia, which can be either squamous or columnar in origin, leads to increased risk of cervical cancer [6]. Conventional practice for diagnosing dysplasia in the lumen of the gastrointestinal tract is endoscopy-guided biopsy with wide-field, broadband illumination followed by histological examination by a pathologist using hematoxylin and eosin (H&E) staining [7–9]. However, diagnosis in this way may be subject to sampling errors and is subjective to the experience of the pathologist, potentially limiting reproducibility [8–10].

One research area that has had success complimenting traditional cancer diagnostic methods is microendoscopy, a flexible endoscopic imaging method capable of providing images of the apical epithelial microenvironment [11]. An established variant of this method, fiber-based high-resolution microendoscopy (HRME) is a non-invasive diagnostic imaging technique that provides sub-cellular resolution images of tissue *in vivo*. Tissue samples are topically stained with a fluorescent contrast agent like proflavine, an acridine-derive fluorescent dye that intercalates DNA. Proflavine highlights cell nuclei with appropriate excitation light to allow visualization of morphological features [12–19]. Other contrast agents, such as benzoporphyrin-derivative monoacid ring A (BPD-MA) and fluorescein, have also been investigated for similar purposes [14]. Generally, excitation light is delivered to the specimen though a coherent image fiber consisting of tens of thousands of individual fibers. The image fiber is placed in direct contact with tissue to excite fluorescent contrast agent and resultant fluorescence is collected by the same image fiber. Lateral and axial resolution are approximately 4 and 20 μm, respectively, with variable fields-of-view depending on the diameter of the image fiber and any distal optics. The primary advantages of HRME are low cost and portability, making this technique clinically translatable [9, 12–18]. Development of these systems has led to clinical studies in the upper and lower gastrointestinal tracts [9, 12, 16, 18] and cervix [13, 15, 17]. However, a limitation of HRME is insufficient depth resolution, minimizing effectiveness in detecting dysplastic changes in the sub-epithelial microenvironment. Only cells on the topmost 20 μm can be visualized and thus some information is lost that would normally be apparent with histopathological analysis [9, 12, 17]. While other microendoscopy methods, such as laser scanning confocal systems, are able to perform axial optical sectioning to resolve cellular structures below the surface, these systems require the use of complex galvanometer or microelectromechanical (MEMS)-based approaches to raster scan the excitation source across the surface of the tissue [20–22]. Fiber bundle microendoscopy, as described in this manuscript, does not include these features in favor of increased robustness and decreased cost. An additional limitation of HRME is its

#247300 Received 4 Aug 2015; revised 14 Oct 2015; accepted 14 Nov 2015; published 19 Nov 2015

inability to quantify changes in tissue scattering and absorption [12–18]. Thus, HRME techniques could benefit from additional quantitative and depth sensitive modalities.

Recent work has described sub-diffuse reflectance spectroscopy (sDRS), which uses short source-detector separations (less than 1 mm) to non-invasively interrogate deeper within epithelia and quantify optical properties [23–29]. Optical properties depend on tissue morphology and can provide a means to quantify dysplastic changes [26]. More specifically, broadband sDRS has been used in multiple clinical studies including quantifying hemoglobin absorption to distinguish between different grades of oral cancer [26], distinguishing between adenomatous colon polyps and normal tissue [27], diagnosing cervical dysplasia *in vivo* [28], and quantifying changes associated with non-melanoma skin cancer [29]. These studies have shown that sDRS can be a useful, non-invasive method to quantify the health of small volumes of tissue although the ability to resolve fine cellular detail with spectroscopy is non-existent [26–29].

To capitalize on advantages provided by these "optical biopsy" methods, we introduce a trimodal, fiber-bundle high-resolution microendoscopy technique with two integrated sub-diffuse reflectance modalities. This technique provides data on 1) high-resolution, image fiber-based fluorescence imaging, 2) broadband, sub-diffuse reflectance spectroscopy (sDRS), and 3) sub-diffuse reflectance intensity mapping (sDRIM) within a single custom fiber bundle [30]. High-resolution, image fiber-based fluorescence images are meant to provide morphological images of the apical cell environment and were acquired by topically staining tissue specimens with proflavine or pyranine ink [19]. Broadband sDRS data are meant to quantify tissue optical properties from a small volume of tissue and were acquired by delivering white light from a tungsten-halogen light source into specimens and collecting spectral information using two discrete source-detector separations (SDS) of 374 and 730 μm. Finally, sDRIM data are meant to provide two-dimensional (2D) spatially-resolved image maps of sub-diffuse reflectance intensity, rather than image features. This data was acquired by delivering red 635 nm laser light to tissue specimens through an off-axis delivery fiber and collecting the reflectance signal with an image fiber [30].

In this manuscript, we describe and validate our instrumentation and present initial proof-of-concept experiments. First, the system was characterized to determine several important imaging specifications including spatial resolution, magnification, percent of maximum field-of-view, and sampling frequency. Second, we quantify the ability to extract optical properties and sampling depth of the sDRS modality. Third, all system modalities were tested on hybrid cell phantoms [31–33] made with poly(dimethylsiloxane) (PDMS) as a substrate material with MDA-MB-468 breast adenocarcinoma cells cultured on the topmost layer. Scattering and absorption of hybrid cell phantoms were tuned by varying concentrations of titanium dioxide and nigrosin, respectively [34]. Next, *in vivo* data were collected from a melanocytic nevus and adjacent normal skin from a volunteer. Qualitative high-resolution fluorescence images were correlated to quantitative data including sub-diffuse reflectance intensity and reduced scattering and absorption coefficient [35]. Finally, the technique was tested on healthy *ex vivo* murine gastrointestinal tissue, similar to other studies using multimodal optical approaches [36, 37]. These pilot studies demonstrate the significance of coupling sDRIM and sDRS modalities to high-resolution fluorescence imaging instrumentation.

2. Materials and methods

2.1 Fiber-optic probe design

The custom fiber-optic probe (Myriad Fiber Imaging, USA) used for this trimodal microendoscopy technique uses five 200/220 μm core/cladding, 0.22 NA multimode fibers (Molex Inc., USA) surrounding a 1 mm Fujikura image fiber (Myriad Fiber Imaging, USA) for a total of six fibers. The central 1 mm image fiber contains approximately 50,000 individual fiber elements 4.5 μm in diameter with center-to-center spacing of approximately

4.5 µm. The center-to-center separation between any one of the 200 µm fibers and the image fiber is 864 µm. Therefore, the closest edge of the image fiber to the center of any 200 µm fiber is approximately 350 µm. Similarly, the farthest edge of the image fiber to the center of any 200 µm fiber is approximately 1,350 µm. The centers of each of the 200 µm fibers are separated by 25°. Based on this geometry, center-to-center SDS between adjacent 200 µm fibers with respect to the leftmost fiber are 374, 730, 1,051, and 1,323 µm. For the purposes of this paper, only the first two SDSs (374 and 730 µm) were used for sDRS measurements. The total length of the fiber-optic probe is 4 ft. in which the distal 2 ft. of the fiber-optic probe consists of a single probe tip 3 mm in diameter and the proximal 2 ft. of the fiber-optic probe, nearest the optical instrumentation, splits into six individual fibers corresponding to each fiber within the bundle. Each of the six fibers ends in an SMA905 connector and can be readily coupled to the microendoscopy instrumentation. Figure 1 shows the details of the fiber-optic probe [30].

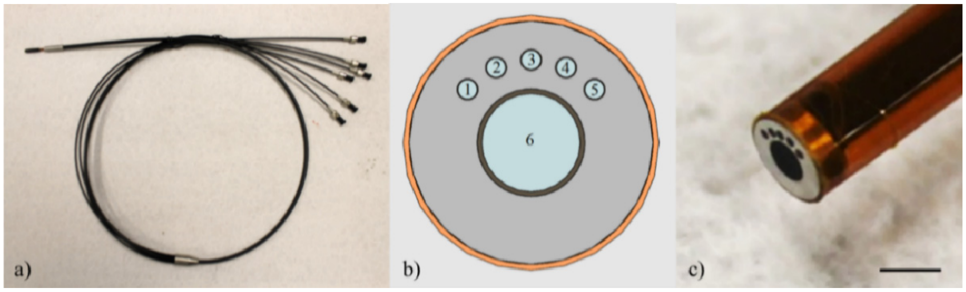

Fig. 1. Fiber-optic probe showing **(a)** the full length (4 ft.) of the probe with the single bundle at the distal end and splitting into six individual bundles at the proximal end, **(b)** a schematic of the probe tip with the central 1 mm image fiber (#6) surrounded by five 200 µm multimode fibers (#1-5) separated by 25°. SDS between fiber #1 and the four adjacent fibers (#2-5) are 374, 730, 1051, and 1323 µm, respectively, and **(c)** close-up of the distal end of the fiber-optic probe (scale bar = 2 mm).

2.2 Instrumentation design

Three light sources, corresponding to the three optical modes of the instrumentation, are delivered to the sample via the custom fiber-optic probe: an LED light source (Philips, USA) centered at 455 nm (20 nm FWHM), a broadband tungsten-halogen white light source (Ocean Optics, USA), and a 635 nm laser (Thorlabs, USA).

For the first mode (high-resolution, image fiber-based fluorescence imaging), light from the 455 nm LED passes through a 460 nm short pass excitation filter (Chroma Technology Corp., USA) and is directed into the back aperture of a 10X/0.30 NA infinity-corrected objective lens (Olympus Corp., Japan) using a 475 nm cut-off dichroic mirror (Chroma Technology Corp., USA). 455 nm excitation light passes through the 1 mm image fiber to the distal end of the probe, illuminating the sample with 1 mW of power. Samples fluorescently stained with proflavine excite in this wavelength range and emit light centered at approximately 515 nm which is collected by the image fiber [19]. Emission light passes through the 475 nm dichroic mirror and is reflected by a second dichroic mirror with a cut-off wavelength of 590 nm (Chroma Technology Corp., USA). This reflected emission light (centered at 515 nm) then passes through a 525/40 nm emission bandpass filter (Chroma Technology Corp., USA), a 50 mm tube lens (Thorlabs), and into an 8-bit, Flea3 USB 3.0 monochrome CMOS camera (Point Grey, Canada) [9, 12–18, 30]. The CMOS camera thus provides magnified apical cell morphological data from the 1 mm-diameter field-of-view (FOV).

For the second mode (broadband sDRS), broadband light (450-750 nm) from the tungsten-halogen lamp is coupled into one 200 µm fiber (fiber #1 from Fig. 1) of the fiber-optic probe to deliver white light to the sample. The wavelength range is limited by the output of the tungsten-halogen source lamp. Sub-diffusely reflected light is collected by two adjacent 200 µm fibers (fiber #2 and #3 from Fig. 1) with corresponding center-to-center SDS of 374 and 730 µm and delivered to a single visible-to-near infrared spectrometer (Ocean Optics, USA) with a spectral resolution of 0.36 nm. A custom designed motorized optical fiber switch allows the spectrometer to sequentially acquire from each collection fiber [30].

For the third mode (sDRIM), the 635 nm laser is coupled into one 200 µm fiber (fiber #5 from Fig. 1) of the fiber-optic probe to deliver light to the sample. Within the sample, laser light undergoes multiple scattering events and emitted light is collected by the central 1 mm image fiber [23, 38]. This emitted 635 nm light passes through both the 475 and 590 nm cut-off dichroic mirrors before being reflected by a 1-inch aluminum mirror (Thorlabs, USA). The collected 635 nm light then passes through a 610 nm long pass emission filter (Chroma Technology Corp., USA), a 50 mm tube lens (Thorlabs, USA), and into a second 8-bit, Flea3 USB 3.0 monochrome CMOS camera (Point Grey, Canada). A second camera is necessary so the resultant 2D sub-diffuse reflectance image maps have the same FOV and image area as the apical cell morphological data and thus can be directly compared. Both CMOS cameras presented here have a sensor array of 2080 x 1552 pixels 2.5 µm wide, a corresponding sensor size of 5.2 x 3.9 mm, and a dynamic range of 62.9 dB [30].

All modalities of the instrumentation are controlled with custom LabVIEW software (National Instruments, USA). Figure 2 shows a schematic of the fiber-bundle microendoscopy system along with images of the physical bench-top instrumentation.

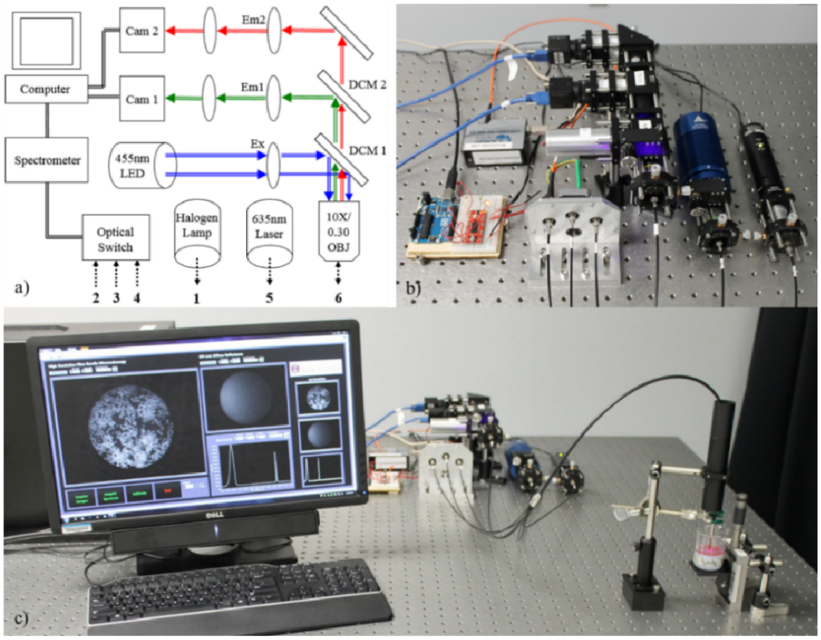

Fig. 2. The trimodal microendoscope showing **(a)** a schematic illustrating major components. 455 nm light passes through a 460 nm short pass excitation filter (Ex). Emitted signal passes through a 10X objective, 475 nm dichroic mirror (DCM1), 525/40 nm emission filter (Em1), and into a camera (Cam 1). 635 nm sDRIM signal passes through the objective lens, 475 (DCM1) and 590 nm dichroic mirrors (DCM2), 610 long pass filter (Em2), and into a camera (Cam 2). An optical fiber switch delivers reflected broadband light from the tungsten halogen lamp to a spectrometer. Finally, **(b)** shows a close-up of the optical components and **(c)** shows the optical components and custom LabVIEW software acquiring data from a hybrid cell phantom.

2.3 System characterization

The instrumentation was characterized to determine the following specifications: 1) spatial resolution, 2) magnification, 3) percent of maximum field-of-view, and 4) sampling frequency. These values were determined with three objective/tube lenses with focal lengths of 50, 100, and 150 mm. For each lens, a 10X/0.30 NA infinity-corrected objective lens was used. Next, the ability of the sDRS modality to extract optical properties (absorption and reduced scattering coefficients) was quantified using a lookup table (LUT) approach [39, 40] Finally, sampling depth was determined for the broadband sDRS modality [25].

First, spatial resolution and maximum field-of-view (FOV) was determined by the geometry of the fiber-optic probe. The image fiber consists of approximately 50,000 individual 4.5 μm-diameter fiber elements with center-to-center spacing of 4.5 μm. The probe is placed in direct contact with a sample; therefore, the optimal spatial resolution that can be achieved is 4.5 μm. In addition, the maximum FOV was approximately 0.8 mm^2, which was determined by the diameter (≈1 mm) of the image fiber. Depending on the objective/tube lens configuration, values for magnification, percent-of-maximum FOV, and sampling frequency vary.

A positive 1951 USAF resolution test target was back-illuminated with a white LED and imaged at group 3/element 3 (linewidth = 49.50 μm) with three tube lenses (focal lengths = 50, 100, and 150 mm). The number of image sensor pixels per micron within the images was then computed. This number was multiplied by the width of the individual pixels (2.5 μm/pixel) to obtain magnification. Percent of maximum FOV was determined by dividing the sampled area projected onto the image sensor by the maximum FOV (0.8 mm^2). Finally, sampling frequency was determined by multiplying the individual fiber element diameter (4.5 μm) by the number of pixels per micron within the images. Equations for obtaining spatial resolution, magnification, percent of maximum FOV, and sampling frequency are shown below as Eq. (1), Eq. (2), Eq. (3), and Eq. (4), respectively. In the following equations, *R* is spatial resolution, *D* is diameter of individual fiber elements (4.5 μm), *M* is magnification, *N* is the number of pixels per micron, *W* is pixel width (2.5 μm), *FOV* is percent of maximum field-of-view, *A* is area, and *F* is sampling frequency.

$$R(\mu m) = D_{fibers}\left(\frac{\mu m}{fiber}\right) \bullet fiber \tag{1}$$

$$M = N_{pixel}\left(\frac{pixel}{\mu m}\right) \bullet W_{pixel}\left(\frac{\mu m}{pixel}\right) \tag{2}$$

$$FOV(\%) = \frac{A_{sample}\left(\mu m^2\right)}{A_{\max imum}\left(\mu m^2\right)} \tag{3}$$

$$F_{sampling} = D_{fiber}\left(\frac{\mu m}{fiber}\right) \bullet N_{pixel}\left(\frac{pixel}{\mu m}\right) \tag{4}$$

Next, extraction of the optical properties, reduced scattering (μ_s') and absorption (μ_a) coefficients, using the sDRS modality was quantified using previously described lookup table-based methods [35, 39, 40]. In summary, 10 calibration phantoms with known optical properties, calculated using Mie Theory (scatting properties) and Beer's Law (absorption properties), were built using distilled water, 1 μm-diameter polystyrene microspheres (07310-15, Polysciences, USA), and a combination of yellow, red, and blue food dye (McCormick & Company, USA). From these phantoms, sub-diffuse reflectance spectral measurements were taken to produce a relationship between reflectance and calculated values of μ_s' and μ_a across the wavelength range of 450-750 nm. With this information, three-dimensional (3D) lookup

#247300 Received 4 Aug 2015; revised 14 Oct 2015; accepted 14 Nov 2015; published 19 Nov 2015

tables (LUT) were built relating μ_a (x-axis), μ_s' (y-axis), and reflectance (z-axis). One LUT was built for each SDS (374 and 730 μm). Continuous ranges of theoretical optical properties were μ_s' = 4.4 to 28.0 cm^{-1} and μ_a = 0.0 to 28.0 cm^{-1}. It was found that 10 calibration phantoms were sufficient to span this continuous range of μ_s' and μ_a. LUTs were validated by creating a set of 27 validation phantoms with known optical properties, and using the LUTs to extract μ_s' and μ_a. These values were compared to theoretical μ_s' and μ_a calculated using Mie Theory and Beer's Law for the validation phantoms. The LUTs were considered sufficient when average percent errors of μ_s' and μ_a extraction for both SDSs (374 and 730 μm) were less than 10%. These validated LUTs can then be used to extract *in vivo* optical properties from tissue with unknown optical properties [29, 35, 39, 40], and is demonstrated on a pilot *in vivo* skin study presented later. To extract *in vivo* optical properties, the absorption spectra of known tissue absorbers, such as melanin and oxygenated and deoxygenated hemoglobin, is required. For this study, widely accepted absorption spectra for these tissue absorbers was used [41, 42].

Next, sampling depth in sDRS-related instrumentation is generally quantified using either computational or empirical methods [24, 25, 43, 44]. In this study, we perform an established empirical method to estimate our sDRS sampling depth range for both SDSs (374 and 730 μm) [25]. For this study, two phantoms were constructed using distilled water, 1 μm-diameter polystyrene microspheres (07310-15, Polysciences, USA), and a combination of yellow, red, and blue food dye (McCormick & Company, USA). The optical properties, μ_s' and μ_a, were calculated using Mie Theory and Beer's Law, respectively. The first phantom had high scattering (μ_s' = 40 cm^{-}1) and high absorption (μ_a = 45 cm^{-1}) at a wavelength of 450 nm. The second phantom had low scattering (μ_s' = 4.4 cm^{-1}) and low absorption (μ_a = 0 cm^{-1}) at a wavelength of 750 nm. The two phantoms were dispensed inside non-reflective, blackened beakers and the probe tip was placed inside so it was in direct contact with the absorbing beaker bottom. The distance between the beaker bottom and probe tip was then manually varied between 0 and 2 mm in 50 μm increments and sDRS data was taken at each increment [25]. At a "semi-infinite" distance between the beaker bottom and probe tip (< 2 mm), each combination of μ_s' and μ_a results in a maximum reflectance intensity. Sampling depth is then defined as the depth in which 50% of photons at a single wavelength reach the bottom, non-reflective, blackened layer (50% maximum reflectance intensity), as shown in Eq. (5). The hypothesis for this experiment was that minimum sampling depth would occur at the maximum tested μ_s' (40 cm^{-1}) and μ_a (45 cm^{-1}) and maximum sampling depth would occur at minimum tested μ_s' (4.4 cm^{-1}) and μ_a (0 cm^{-1}). Furthermore, sampling depth for the 730 μm SDS was expected be greater than sampling depth for the 374 μm SDS [25]. In the following equation, D_s is sampling depth, d is distance of probe tip to beaker bottom (50 μm increments), I_{max} is maximum reflectance intensity, μ_s' is reduced scattering coefficient and μ_a is absorption coefficient.

$$D_s\left(\mu_s^{'},\mu_a\right)=\frac{1}{2}\left[d_{I_{\max}\left(\mu_s^{'},\mu_a\right)}\right] \tag{5}$$

2.4 Hybrid cell phantoms

To demonstrate the three modalities, two hybrid cell phantoms were constructed using PDMS as a substrate material and titanium dioxide (Sigma Aldrich, USA) and nigrosin (Sigma Aldrich, USA) as the scattering and absorbing agents, respectively [34]. Both phantoms consisted of a 2.5 cm thick layer containing a scattering concentration of 8.0 mg/g TiO_2/PDMS and absorbing concentration of 5.0 μL/g 1% w/v distilled nigrosin/PDMS. The second phantom consisted of an additional 500 μm thin absorbing layer which had had a scattering concentration of 8.0 mg/g TiO_2/PDMS and absorbing concentration of 10.0 μL/g 1% w/v distilled nigrosin/PDMS [34].

After curing, hybrid cell phantoms were autoclaved and MDA-MB-468 breast adenocarcinoma cells were cultured on top. MDA-MB-468 breast adenocarcinoma cells (ATCC, USA) were cultured up to the fourth passage in Dulbecco's Modified Eagle Medium (DMEM) (ATCC, USA) containing 10% fetal bovine serum (ATCC, USA) and 5% antibiotics (Sigma Aldrich, USA) at 37°C in 5% CO_2. 24 hours after passaging, 200,000 cells in 4 mL DMEM were seeded onto the phantoms. Each phantom was then transferred to the fiber-optic probe tip. A 0.01% w/v solution (1 mL) of proflavine in saline was added to the cell culture media to provide fluorescent contrast of the nuclei [19]. The 455 nm LED and 635 nm laser provided optical powers at the sample plane of 1.00 mW and 0.25 mW, respectively. Both high-resolution fluorescence and sDRIM data were collected simultaneously. sDRIM data were quantified by using a MATLAB script to compute a line plot through the center of the image circle and plotting intensity over continuous SDS between 400 and 1,300 µm. Ten raw sDRIM images were averaged. Immediately following this, the tungsten-halogen lamp delivered 0.35 mW of power at the sample plane. Broadband sDRS measurements were then acquired at both tested SDSs of 374 and 730 µm. For this experiment, both cameras were set to an exposure time of 150 ms and gain of 10 dB. The spectrometer had an integration time of 0.5 s and boxcar width [45] of 3. Three spectra were averaged at each SDS for both hybrid phantoms.

The hypothesis for this experiment was that there would be no discernable difference between high-resolution image data of cultured MDA-MB-468 breast adenocarcinoma cells between the two phantoms, but differences would be seen in the reflectance intensities for sDRIM and sDRS data due to the underlying absorbing layer. Table 1 shows specifications for all phantom layers.

Table 1. Specifications for non-biological components of hybrid tissue-simulating phantoms

Phantom Number	1 (single-layer)		2 (double-layer)	
Layer	Bottom	Top	Bottom	Top
Thickness (mm)	25	0	25	0.5
[Scattering] (mg/g TiO_2/PDMS)	8.0	0	8.0	8.0
Estimated μ_s' (cm^{-1})	10.0	0	10.0	10.0
[Absorption] (µL/g dist. Nigrosin/PDMS)	5.0	0	5.0	10.0
Estimated μ_a (cm^{-1})	1.0	0	1.0	2.0

2.5 In vivo human melanocytic nevus

The trimodal technique was tested on a selected benign melanocytic nevus and adjacent normal skin from a healthy Caucasian volunteer. All procedures were approved by the University of Arkansas Institutional Review Board (IRB #15-09-149). A benign melanocytic nevi was chosen as a demonstration because of its similar cellular arrangement to surrounding normal tissue. Contributions from melanin cannot be discerned using high-resolution fluorescence imaging, but these highly absorbing contributions become apparent when using the integrated sub-diffuse reflectance modalities, sDRIM and sDRS [46, 47].

Highlighter ink, which contains the fluorescence compound, pyranine, was applied to the skin instead of proflavine. Excitation of pyranine was accomplished using the 455 nm LED as the excitation source, similar to proflavine. However, unlike proflavine, pyranine does not intercalate DNA and thus preferentially stains cell membranes rather than nuclei. The probe tip was placed in direct contact with the skin surface while the 455 nm LED, 635 nm laser, and tungsten-halogen lamp provided optical powers of 1.00 mW, 0.25 mW, and 0.35 mW, respectively. Both high-resolution fluorescence imaging and sDRIM data were collected with an exposure time of 150 ms and gain of 10 dB whereas broadband sDRS data used an integration time of 500 ms and boxcar width of 3 [45]. Ten high-resolution fluorescence

#247300 Received 4 Aug 2015; revised 14 Oct 2015; accepted 14 Nov 2015; published 19 Nov 2015

images, ten sDRIM data, and three sDRS data were acquired from each site. The best qualitative high-resolution fluorescence image was selected while ten sDRIM and three sDRS data were averaged together. After acquisition, the LUT-based inverse model was used to extract μ_s' and μ_a (@ 630 nm) from the *in vivo* sDRS data of the melanocytic nevus and adjacent normal skin tissue [29, 35, 39, 40].

The hypothesis for this experiment was that there would be no discernable difference between high-resolution image data between the keratinocytes of the benign melanocytic nevus and surrounding tissue, but differences would be seen in the reflectance intensities for sDRIM and sDRS data due to increases in melanin concentration.

2.6 Ex vivo murine colon tissue

As a demonstration of technique in a murine model, a 16-week old wild-type (C57BL/6J) mouse (Jackson Laboratories, USA) was housed in a room with a 16:8-hour light-dark cycle and had access to standard rodent food (8640 Teklad 22/5 Rodent Diet, Harlan Sprague Dawley Inc., USA) and water ad libitum. Seven days prior to data collection, the mouse was switched to a 50/50 mix of standard rodent food and purified food (AIN-93G Purified Diet, Harlan Sprague Dawley Inc., USA). The mouse was switched to 100% purified food four days prior to data collection and no food 24 hours prior. All procedures were approved by the University of Arkansas Institutional Animal Care and Use Committee (IACUC, #15009) [48–50].

A 1 cm^2 square section of colonic tissue (4-5 cm from anus) was isolated. A segment of this tissue site was immediately placed in 10% formalin for 24 hours for fixation prior to H&E staining. The 4-5 cm section was placed lumen-side up on a solid PDMS-based phantom. An underlying PDMS-based phantom was used to eliminate transmitted light because of the thinness of tissue (≈200 μm thick) [51–53]. The phantom had a refractive index of 1.4 to match that of tissue to avoid artifacts due to Fresnel reflection and contained 1% w/v nigrosin/EtOH (5.0 μL/g PDMS, $\mu_a \approx 1.0\ cm^{-1}$ at 635nm) and TiO_2 (8.0 mg/g PDMS, $\mu_s' \approx 10\ cm^{-1}$ at 635nm) to approximate the optical coefficients of colonic tissue at 635 nm [32, 54–58].

Cold PBS at 4°C was used to keep tissue moist throughout data collection which took place within an hour after time of death. A 4°C, 0.01% w/v solution (1 mL) of proflavine in saline was topically applied to the tissue sample immediately prior to data collection. The 455 nm LED, 635 nm laser, and tungsten-halogen lamp provided optical powers at the sample plane of 1.00 mW, 0.25 mW, and 0.35 mW, respectively. High-resolution fluorescence imaging and sDRIM data were collected with an exposure time of 150 ms and gain of 10 dB whereas broadband sDRS data used an integration time of 500 ms and boxcar width of 3 [45].

Ten high-resolution fluorescence images, ten sDRIM data, and three sDRS data were acquired from the colon section. The best qualitative high-resolution fluorescence image was selected for comparison to H&E while the ten sDRIM and three sDRS data were averaged.

3. Results

3.1 System characterization

Figure 3 shows images taken of a positive 1951 USAF resolution test target at group 3/element 3 (linewidth = 49.50 μm). These images were used to quantify spatial resolution, magnification, percent maximum FOV, and sampling frequency, listed in Table 2. The 50 mm tube lens (Fig. 3(a)) was chosen for use with the 10X/0.30 NA infinity-corrected objective lens for data collection because of the desirable percent maximum FOV (%) and sampling frequency (pixels/fiber element) which were 100% and 5.4, respectively. This configuration maximizes the field-of-view while satisfying the Nyquist sampling requirement.

#247300 Received 4 Aug 2015; revised 14 Oct 2015; accepted 14 Nov 2015; published 19 Nov 2015

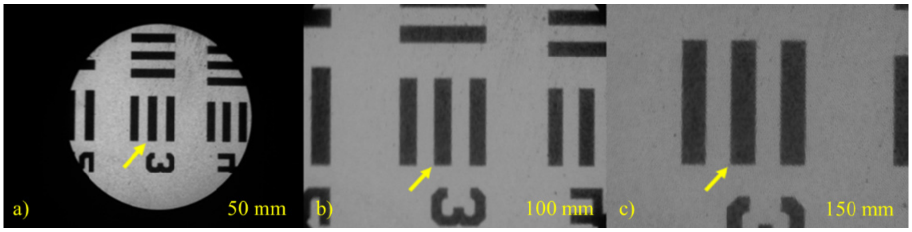

Fig. 3. Images of group 3/element 3 (linewidth = 49.50 µm) of a positive 1951 USAF resolution test target taken with a 10X/0.30 NA infinity-corrected objective lens and tube lenses with focal lengths of **(a)** 50 mm, **(b)** 100 mm, and **(c)** 150 mm. The yellow arrow points to the same target on each image.

Table 2. System specifications for the high-resolution modality with different tube lenses

Focal Length of Tube Lens	50 mm	100 mm	150 mm
Spatial Resolution [µm]	4.5	4.5	4.5
Image sensor pixels/µm [pixels/µm]	1.21	2.65	3.61
Magnification on CCD sensor	3.0	6.6	9.0
Percent of Maximum FOV	100%	56%	30%
Sampling Frequency [pixels/fiber]	5.4	11.9	16.2

For the sDRS modality, 3D LUTs were generated based on a set of 10 calibration phantoms for both SDSs (374 and 730 µm). These LUTs were validated with 27 validation phantoms. Figure 4 shows the LUT for the 374 µm SDS with superimposed raw reflectance data from the validation phantoms. The validation phantom reflectance data overlaid the LUT well, and minor discrepancies contribute to percent errors when comparing extracted optical properties with theoretical optical properties of the validation phantoms. The comparison of extracted and theoretical μ_s’ is shown in Fig. 4(b) and the comparison of extracted and theoretical μ_a is shown in Fig. 4(c). Taking into account all validation phantom data from Fig. 4(a), the 374 µm SDS of the sDRS modality can extract μ_s’ and μ_a with average percent errors of 4.7% and 9.5%, respectively. Similarly, the 730 µm SDS of the sDRS modality can extract μ_s’ and μ_a with average percent errors of 4.0% and 8.3%, respectively. To match tolerance levels presented in similar studies, our goal was to reduce average percent errors below 10% across the range of validated optical properties presented here.

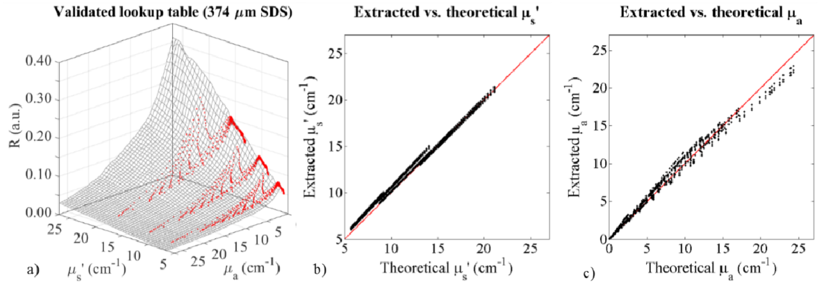

Fig. 4. Characterization of the 374 µm SDS sDRS modality of the trimodal instrumentation. This figure shows (a) a LUT (black mesh) generated by a set of 10 calibration phantoms describing reflectance (R) as a function of μ_s’ (4.4-27 cm^{-1}) and μ_a (0-27 cm^{-1}) with superimposed reflectance data (red dots) from the 27 validation phantoms. Discrepancies between the LUT and validation phantoms contribute to percent error in the ability of the LUT to extract optical properties. Additionally, this figure shows (b) extracted (via LUT inverse model) vs. theoretical (via Mie Theory) μ_s’ of the 27 validation phantoms with a perfect fit line (red), and (c) extracted (via LUT inverse model) vs. theoretical (via Beer’s Law) μ_a of the 27 validation phantoms with a perfect fit line (red). Discrepancies between extracted and theoretical values contribute to percent error.

#247300 Received 4 Aug 2015; revised 14 Oct 2015; accepted 14 Nov 2015; published 19 Nov 2015

In addition to quantitative optical property extraction via sDRS, sampling depth was also estimated in two liquid phantoms (high scattering/absorption and low scattering/absorption). The estimated minimum sampling depths (50 μm increments) for the 374 μm and 730 μm SDSs were 150 and 250 μm, respectively. The estimated maximum sampling depths (50 μm increments) for the 374 μm and 730 μm SDSs were 500 and 700 μm, respectively. These findings were comparable to similar studies and supported our hypothesis that minimum sampling depth would occur at the maximum tested μ_s' (40 cm^{-1}) and μ_a (45 cm^{-1}) and maximum sampling depth would occur at minimum tested μ_s' (4.4 cm^{-1}) and μ_a (0 cm^{-1}) [25]. Furthermore, our hypothesis was supported by the 730 μm SDS having a greater sampling depth compared to the 374 μm SDS [25]. Percent errors for optical property extraction and estimated sampling depths are organized in an easy-to-read specifications table, shown in Table 3.

Table 3. System specifications for the sDRS modality with two source-detector separations

Source-Detector Separation (SDS)	**374 μm**	**730 μm**
Average Percent Error for μ_s' Extraction (%)	4.7%	4.0%
Average Percent Error for μ_a Extraction (%)	9.5%	8.3%
Estimated Minimum Depth (μm) @ $\mu_s' \approx 40\ cm^{-1}$, $\mu_a \approx 45\ cm^{-1}$	150	250
Estimated Maximum Depth (μm) @ $\mu_s' \approx 4.4\ cm^{-1}$, $\mu_a \approx 0\ cm^{-1}$	500	700

3.2 Hybrid cell phantoms

A representation of the hybrid cell phantoms are shown in Fig. 5(a), 5(d). Sample data from the high-resolution, fiber-based fluorescence imaging modality are shown for both hybrid cell phantoms in Fig. 5(b), 5(e). sDRIM data are shown in Fig. 5(c), 5(f) and the quantification of these maps is shown in Fig. 5(g). sDRIM data were quantified by using a MATLAB script to take a line plot through the center of the image circle and plotting intensity (in pixel values) over continuous SDS between 400 and 1,300 μm. Finally, broadband sDRS data for both SDSs (374 and 730 μm) from both hybrid cell phantoms are shown in Fig. 5(h), 5(i).

Our hypothesis was supported. There was no discernable difference between high-resolution image data of cultured breast adenocarcinoma cells between the two phantoms, but clear differences were seen in reflectance for the sDRIM and sDRS data. sDRIM data shows greater signal closer to the 635 nm source delivery fiber, and intensity is markedly reduced for the double-layer phantom containing the more highly absorbing underlying layer. The overall shape of the sDRIM profiles remains similar between samples, as expected. The shape of sDRIM profiles are similar to those predicted by established Monte Carlo models of reflectance [59]. For the sDRS data, intensity changes are due to increases in nigrosin concentration, which have a flat absorption spectra across the tested wavelengths [34]. Also note that for the 730 μm SDS, there are increased reflectance contributions from longer wavelengths when compared to the 374 μm SDS, consistent with the 730 μm SDS sampling a greater depth range [25].

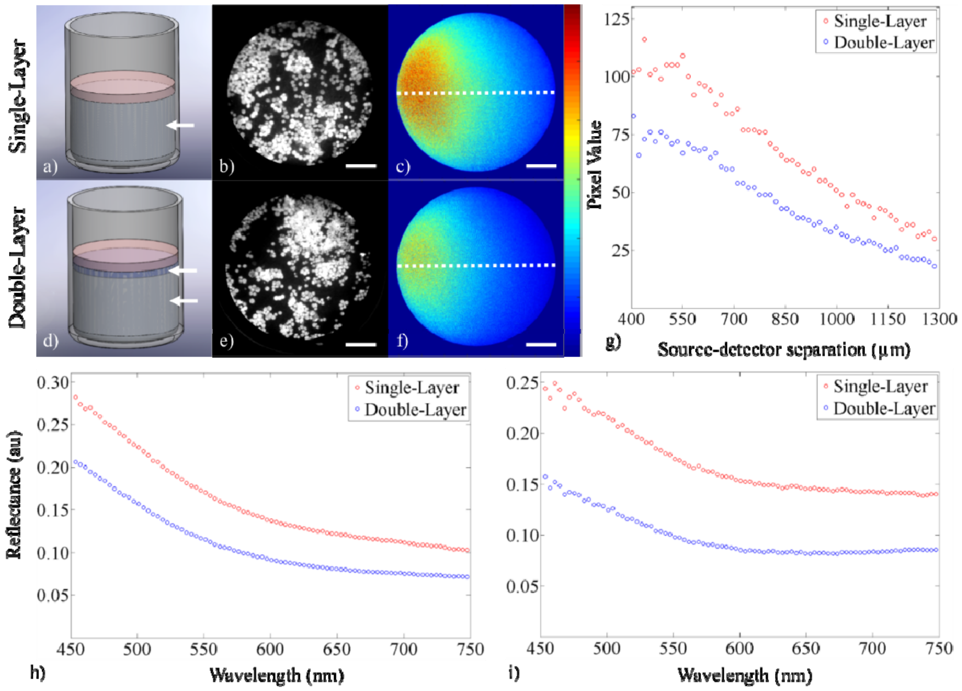

Fig. 5. Demonstration of the three modalities showing data from the hybrid cell phantoms containing **(a-c)** one or **(d-f)** two layers. The figure shows **(a, d)** a SolidWorks representation of the single and double layer hybrid cell phantoms (with white arrows pointing at layers), **(b, e)** enhanced high-resolution fluorescence images after topical staining of MDA-MB-468 breast adenocarcinoma cells with proflavine (scale bar = 225 µm), **(c, f)** sDRIM data (scale bar = 225 µm, color bar = 0-130), **(g)** quantification of the sDRIM data taken across the face of the image fiber (400-1,300 µm SDS from laser source), **(h)** broadband sDRS data (374 µm SDS), and **(i)** broadband sDRS data (730 µm SDS).

3.3 In vivo human melanocytic nevus

For the healthy skin tissue and adjacent melanocytic nevus, data were collected for all three modalities, shown in Fig. 6. A DSLR image of both tissue sites is shown in Fig. 6(a), 6(d) alongside the high-resolution fluorescence image (Fig. 6(b), 6(e)), sDRIM data (Fig. 6(c), 6(f), 6(g)), and broadband sDRS at both SDSs of 374 and 730 µm (Fig. 6(h), 6(i)).

Our hypothesis was supported. There were no discernable differences between high-resolution image data between the keratinocytes of the benign melanocytic nevus and surrounding tissue. In addition, differences were seen in sDRIM and sDRS modalities due to increased melanin concentration, contributing to increased μ_a [42].

Keratinocyte morphology can be distinguished in both sites in the high-resolution fluorescence images. Nuclei are not visualized in Fig. 6(b), 6(e) because pyranine-derived ink does not intercalate DNA, and thus only the cell membranes boundaries are visualized.

Next, a comparison of sDRIM data shows markedly different reflectance intensities across the face of the image fiber. The overall shape of the sDRIM profiles remains similar between samples, as expected. The shape of sDRIM profiles are similar to those predicted by established Monte Carlo models of reflectance [59]. Finally, *in vivo* broadband sDRS data was fit using the validated LUT-based model approach as previously described. Raw data (dots) and model fits (lines) are plotted together in Fig. 7(h), 7(i). sDRS data shows Q-bands of hemoglobin at 542 and 577 nm for surrounding healthy tissue, although these Q-bands are masked by melanin contributions in the benign melanocytic nevus. The appearance of the Q-bands in the reflectance spectra indicated that our instrument was sampling into the vascularized dermis [41].

Next, the LUT-based model extracted μ_s' and μ_a from the normal skin and melanocytic nevus for both SDSs (374 and 730 μm). All listed optical properties were referenced at 630 nm. For normal skin, μ_s' was estimated at 16.0 and 11.6 cm^{-1} while μ_a was estimated at 0.9 cm^{-1} for both the 374 and 730 μm SDS, respectively. For the melanocytic nevus, μ_s' was estimated at 23.9 and 28.0 cm^{-1} while μ_a was estimated at 13.8 and 12.3 cm^{-1} for the 374 and 730 μm SDS, respectively. These values for normal skin, as well as the relative increase in both μ_s' and μ_a for the melanocytic nevus, are consistent with previously published results [29, 47, 60–62].

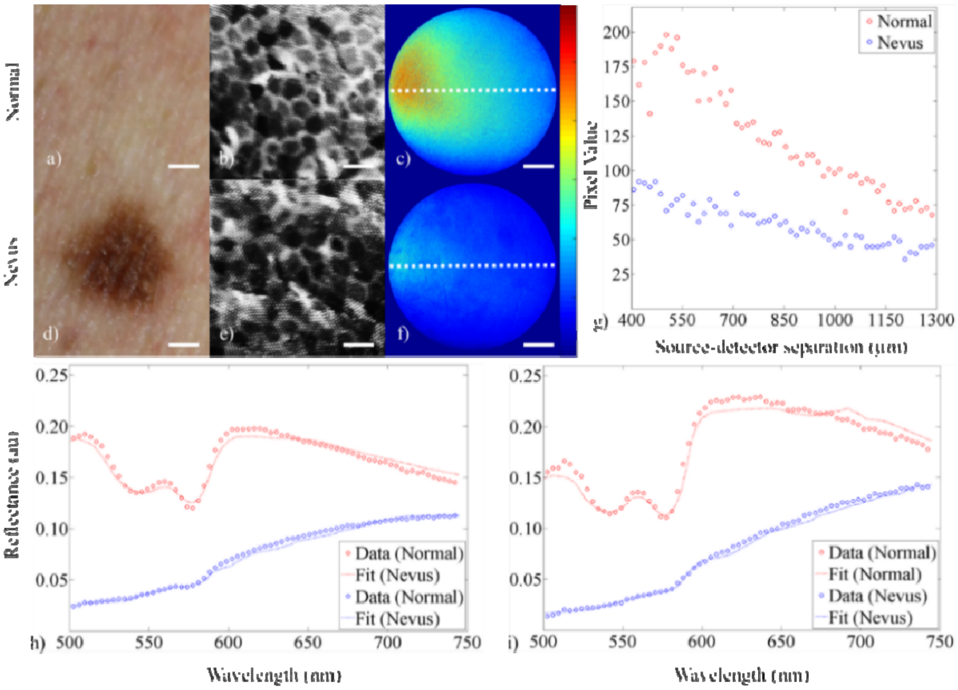

Fig. 6. Demonstration of technique showing data from **(a-c)** human healthy skin tissue and **(d-f)** adjacent melanocytic nevus. The figure shows **(a, d)** a digital image of the healthy skin and adjacent melanocytic nevus (scale bar = 1 mm), **(b, e)** cropped and enhanced high-resolution fluorescence images after topical staining with pyranine-derived highlighter ink (scale bar = 50 μm), **(c, f)** sDRIM data (scale bar = 225 μm, color bar = 0-225), **(g)** quantification of the sDRIM data taken across the face of the image fiber (400-1,300 μm SDS from 635 nm laser source), **(h)** broadband sDRS data (374 μm SDS), and **(i)** broadband sDRS data (730 μm SDS). Raw data are shown as dots and the LUT-based inverse model fits are shown as a curve.

3.4 Ex vivo murine colon tissue

For the healthy (C57BL/6J) mouse, data was collected for all three modalities, shown in Fig. 7. A DSLR image of the resected piece of colon is shown in Fig. 7(a) alongside the associated histology (Fig. 7(b)) and high-resolution fluorescence image (Fig. 7(c)), sDRIM (Fig. 7(d)), and broadband sDRS at both SDSs of 374 and 730 μm (Fig. 7(f), 7(g)). For the sDRIM data, a line plot was taken through the center of each intensity map (Fig. 7(d)) to create a plot of intensity as a function of SDS between 400 and 1,300 μm, shown in Fig. 7(e).

Note the ability to clearly resolve glandular structure in the murine colon alongside spatially resolved sub-diffuse reflectance intensity. For the sDRIM data, the overall shape is similar to previous results presented here with a shape similar to that predicted by Monte Carlo models of reflectance [59]. The Soret bands due to hemoglobin can be clearly

#247300 Received 4 Aug 2015; revised 14 Oct 2015; accepted 14 Nov 2015; published 19 Nov 2015

distinguished from the sDRS data. The Q-bands (542 and 577 nm) are less apparent, most likely due to contributions from the underlying phantom layer. Also note that for the 730 μm SDS, there was increased reflectance contributions from longer wavelengths when compared to the 374 μm SDS. This data demonstrates that data can be acquired from murine colon tissue. Future studies will forego the use of an underlying phantom in *in vivo* studies to elucidate the effectiveness of the sDRIM and sDRS modalities within a larger sample size.

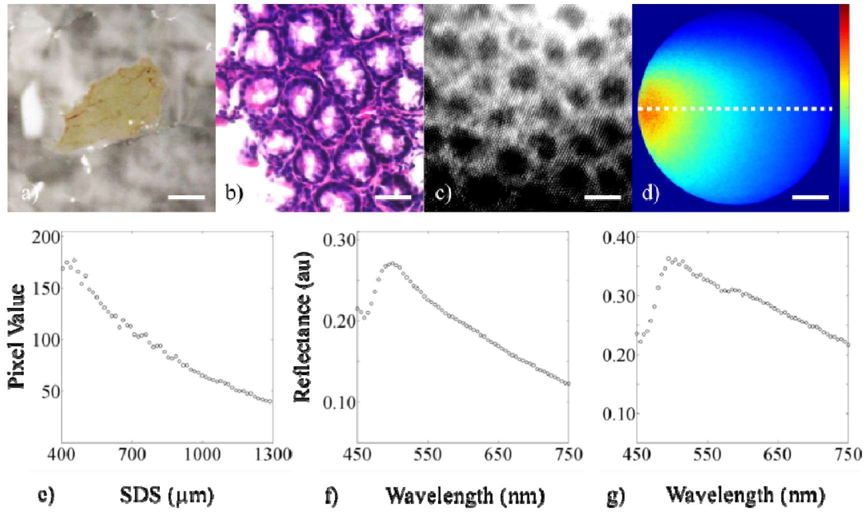

Fig. 7. Demonstration of the three modalities showing data from a 16-week old wild-type (C57BL/6J) male mouse. The figure shows **(a)** digital image of the 4-5 cm colon tissue (lumen side facing up, scale bar = 5 mm), **(b)** histology of an adjacent section (scale bar = 50 μm), **(c)** cropped and enhanced high-resolution fluorescence image after topical staining with 0.01% w/v proflavine (scale bar = 50 μm), **(d)** sDRIM data (scale bar = 225 μm, color bar = 0-200), **(e)** quantification of the sDRIM data taken across the face of the image fiber (400-1,300 μm SDS from 635 nm laser source), **(f)** broadband sDRS data (374 μm SDS), and **(g)** broadband sDRS data (730 μm SDS).

4. Discussion

We have developed a trimodal, fiber-bundle microendoscopy technique that provides data on 1) high-resolution, image fiber-based fluorescence imaging, 2) broadband sDRS, and 3) sDRIM within a single custom fiber bundle. This technique is based around a flexible fiber-optic probe (Fig. 1) and simple optical components (Fig. 2) to collect co-registered qualitative and quantitative information of epithelial tissues.

In this manuscript, we characterize our technique in terms of spatial resolution, magnification, field-of-view, sampling frequency, optical property extraction, and sampling depth (Fig. 3 and 4, Table 2 and 3). The technique was demonstrated in optical phantoms containing cultured MDA-MB-468 breast adenocarcinoma cells (Fig. 5, Table 1), an *in vivo* human melanocytic nevus of the skin (Fig. 6), and *ex vivo* murine colon epithelial tissue (Fig. 7). The validated LUT-based inverse model was used to extract tissue optical properties of the *in vivo* human melanocytic nevus and surrounding healthy skin tissue.

High-resolution fluorescence imaging, using a coherent fiber bundle image fiber, was chosen as the first modality because of its established success in diagnosis of dysplasia in various endoscopically accessible organs. This modality can provide highly-resolved qualitative data regarding structure and morphology of the apical layers of epithelial tissue. However, alone, it lacks the capability of providing functional information and imaging deeply into tissue. To overcome this limitation, broadband sDRS was chosen as a second modality to provide quantitative functional, rather than structural, information at various sampling depth ranges in tissue. Thus, these modalities have great complimentary potential. A

#247300 Received 4 Aug 2015; revised 14 Oct 2015; accepted 14 Nov 2015; published 19 Nov 2015

third modality, sDRIM, was developed to provide 2D, spatially-resolved image maps of sub-diffuse reflectance intensity of the same image area and field-of-view as the high-resolution fluorescence imaging modality. These additionally modalities, sDRS and sDRIM, can collect information below the surface, which wasn't possible with conventional end-on fiber bundle microendoscopy [11–18, 23–30, 35, 39, 40].

Other techniques have attempted to address similar technical limitations. For example, high-resolution imaging techniques have been coupled with wide-field autofluorescence imaging, such as with the commercially available VELscope, to increase field-of-view while increasing diagnostic specificity in dysplastic lesions [63]. However, no functional depth-sensitive information is acquired. Several clinically available systems capable of providing highly resolved morphological information at varying depths are the Pentax ISC-1000 confocal endomicroscopy system (Pentax/Hoya, Japan and Optiscan Pty Ltd, Australia), and the Cellvizio system (Mauna Kea Technology, France), which have the capability of being coupled to conventional video endoscopes for combined widefield and confocal imaging [64]. These commercial systems have significantly increased sensitivity and specific in cancer diagnostics, but still lack the quantitative features that make spectroscopy attractive. Additionally, the scanning optics necessary for such confocal systems can be costly to miniaturize [64]. Our instrumentation design eliminates the need for scanning optics in favor of simple optics that combine high-resolution probe-based fluorescence imaging with additional spectroscopy and reflectance modalities that can be potentially miniaturized for clinical use.

The primary limitation of this current multimodal technique is lack of a widefield imaging modality, and thus, future studies will explore coupling the fiber-optic probe through the biopsy port of a conventional endoscope [64]. This will increase the potential for clinical compatibility. Secondly, a much larger *in vivo* study of murine gastrointestinal tissue will compare differences between mice with and without gastrointestinal dysplasia to evaluate the effectiveness of this technique in a pre-clinical setting [36, 37, 65]. Finally, future studies will compare the monochromatic, 2D sub-diffuse reflectance intensity maps (sDRIM) with Monte Carlo models of photon transport in turbid media to elucidate this modality's effectiveness as a diagnostic tool for dysplasia [59].

5. Conclusion

With this multimodal system, epithelial morphological data can be correlated with quantitative reflectance data of the subsurface microenvironment, including associated optical properties. By using simple optics and a single, custom fiber bundle, this system is potentially clinically translatable.

Acknowledgments

This material is based on work supported by the National Institutes of Health (1R03CA182052-01), the National Science Foundation Graduate Research Fellowship Program (G.G., DGE-1450079), the Arkansas Biosciences Institute (000519-00001), and the University of Arkansas Doctoral Academy Fellowship. Any opinions, findings, and conclusions or recommendations expressed in this material are those of the authors and do not necessarily reflect the views of the acknowledged funding agencies.